Received: 11 November 2025 | Revised: 28 April 2026 | Accepted: 29 May 2026 | Published online: 23 June 2026

RESEARCH ARTICLE

Journal of Optics and Photonics Research
2026, Vol. 00(00) 1–10
DOI: 10.47852/bonviewJOPR62028166

BON VIEW PUBLISHING

Mitigating Surface-Roughness Effects in the $BaTiO_3$ Top Protective Layer of a Divergence Beam Surface Plasmon Resonance Sensor Using Savitzky–Golay and Whittaker Filters

Jordan H. Hossea[1,*] and Athuman O. Mfinanga[1]

[1] *Department of Electronics and Telecommunications Engineering, Dar Es Salaam Institute of Technology, United Republic of Tanzania*

Abstract: Surface roughness in the top protective layer of a surface plasmon resonance (SPR) sensor degrades performance by introducing reflectivity fluctuations, broadening the resonance dip, and reducing the accuracy of resonance-angle estimation. In practice, obtaining a perfectly uniform barium titanate ($BaTiO_3$) protective coating over a commercially sized SPR chip is difficult; therefore, signal processing strategies that compensate for roughness are of practical interest. In this study, a periodic roughness profile is used to model thickness fluctuations in a 3 nm $BaTiO_3$ overlayer, and the resulting impact on SPR performance is analyzed theoretically using the transfer matrix method. Two digital smoothing approaches, the Savitzky–Golay (SG) filter and the Whittaker filter, are then evaluated as post-processing tools. The results show that the roughness height of 1 nm can reduce the signal-to-noise ratio (SNR) to approximately 6.4 dB and broaden the resonance feature sufficiently to compromise reliable detection. Among the tested methods, the Whittaker filter yields the most faithful recovery of the SPR curve, improving resonance-position accuracy by a factor of 119.14 relative to the rough signal, whereas the SG filter provides an improvement factor of 18.81. The Whittaker filter also increases the SNR to 26.44 dB, which signifies enhancement by 75% and preserves sensor sensitivity (390.12°/refractive index unit (RIU)), which remains close to the ideal value of 396.27°/RIU and detection accuracy more effectively than the SG filter. These findings indicate that Whittaker smoothing is a practical, low-cost computational strategy for mitigating roughness-induced degradation in high-sensitivity SPR biosensors.

Keywords: surface plasmon resonance, biosensors, surface roughness, Savitzky–Golay filter, Whittaker filter

1. Introduction

Surface plasmon resonance (SPR) sensors are widely used for label-free and real-time detection in biomedical, environmental, and food-analysis applications because the resonance condition is highly sensitive to refractive-index changes at the metal/analyte interface. Representative applications include cancer biomarker detection, malaria diagnosis, urinary tract infection sensing, tuberculosis screening, nucleic-acid analysis, ribonucleic acid and deoxyribonucleic acid, and food-quality monitoring [1–9].

At a metal–dielectric interface, incident light can excite collective oscillations of free electrons, known as surface plasmons, under an appropriate resonance condition. In prism-coupled SPR, this resonance is observed as a pronounced dip in the reflected intensity, and the angular position of that dip shifts when the refractive index (RI) of the sensing medium changes. Consequently, accurate determination of the resonance angle is central to SPR sensing because the dip position, width, and depth collectively govern sensitivity, detection accuracy (DA), and resolution [10].

Among the two classical attenuated total reflection configurations used to excite SPR, the Kretschmann geometry is more practical than the Otto geometry because it does not require a precisely maintained nanometer-scale air gap. In the Kretschmann arrangement, a thin metal film is deposited directly on the prism, allowing the evanescent field to couple efficiently into surface plasmons at the outer metal interface. Owing to its mechanical simplicity and experimental robustness, the Kretschmann configuration has become the standard platform for most contemporary SPR devices.

For angular interrogation, conventional mechanical scanning systems can cover a broad range of incidence angles, but they are vulnerable to motor-resolution limits, alignment errors, walk off, and thermal instability. A divergent-beam configuration offers an attractive alternative because a bundle of rays spanning multiple incidence angles simultaneously illuminates the sensing structure. When generated with a Powell lens or cylindrical optics,

***Corresponding author:** Jordan H. Hossea, Department of Electronics and Telecommunications Engineering, Dar Es Salaam Institute of Technology, Tanzania. Email: jordan.hossea@dit.ac.tz

the divergent beam can support wide-angle interrogation without mechanical scanning, thereby improving compactness, stability, and acquisition speed [11, 12].

For the metallic SPR-active layer, silver is selected over gold for its higher sensitivity and sharper resonance, which are critical for achieving high-resolution measurements. To overcome silver's inherent susceptibility to oxidation in aqueous or biological media, the surface is passivated with a thin film of indium tin oxide (ITO) [13], zinc oxide (ZnO) [14], zirconium oxide (ZrO_2) [15], silicon (Si) [16], titanium oxide (TiO_2) [17], gold layer [15], graphene [18], and barium titanate ($BaTiO_3$) [19–23], improving the SPR sensor performance while ensuring chemical stability. $BaTiO_3$ is extensively utilized among protective overlayers due to its advantageous combination of a high RI and low dielectric loss, which generates a robust localized electric field that significantly improves sensor performance by inducing a considerable resonance shift for minor fluctuations in the analyte's RI [20, 24]. However, the use $BaTiO_3$ was under assumption that the thickness of the $BaTiO_3$ is smooth, in which when it was coated on of commercially available SPR sensor chip with sizes such as 20×20 mm^2 manufactured by NanoSPR (BA1000; NanoSPR), $19.5 \times 19.5 \times 1.1$ mm manufactured by Geomatec (Wuxi) Co. Ltd. (China), and 13×20 mm manufactured by Nippon Laser & Electronics Lab (Nagoya, Japan), the possibility to fabricate SPR sensor with smooth top protective layer will be nearly impossible.

Although $BaTiO_3$ is a theoretically promising protective layer, its optimal performance is contingent upon the deposition of a perfectly smooth film. Achieving this uniformity on commercially available, centimeter-scale sensor chips—including models from NanoSPR (BA1000; 20×20 mm^2), Geomatec Co. Ltd. (19.5×19.5 mm^2), and Nippon Laser & Electronics Lab (13×20 mm)—is a formidable practical limitation. Variations in $BaTiO_3$ film roughness on the scale of nanometers can degrade sensor performance. While prior research has extensively examined the impact of surface roughness in the metallic layer or coupling prism on SPR sensor performance, two critical gaps remain unaddressed [25–29]. First, the specific influence of roughness in the top protective overlayer, which is a crucial component for stability and enhancement, has not been systematically investigated. Second, existing literature lacks proposed strategies to mitigate the detrimental effects of such roughness on sensor response.

To address this gap, the present work investigates how surface roughness in a $BaTiO_3$ protective overlayer modifies the SPR response of a divergence-beam sensor and examines whether digital filtering can recover an interpretable resonance signature without changing the sensor hardware.

The novel contributions of this work are threefold: first, a periodic roughness model is introduced to represent practical thickness variations in a 3 nm $BaTiO_3$ overlayer; second, to analytically characterize the impact of top-layer $BaTiO_3$ roughness on SPR sensor performance, and third, to propose and compare two digital filter algorithms—the Whittaker smoother and the Savitzky–Golay filter as effective post-processing tools to mitigate these effects. We demonstrate that such algorithmic compensation can significantly enhance sensitivity, improve resolution, and sharpen the resonance dip (full width at half maximum (FWHM)), thereby reducing the need for costly ultra-precision instrumentation in the SPR sensor chip fabrication process. A detailed comparative analysis establishes the relative merits of each filter, providing a practical framework for enhancing the cost-performance ratio of SPR sensors.

2. Literature Review

In practice, coating $BaTiO_3$ on top of Ag does not guarantee a perfectly uniform film over the full area of an SPR chip. Even when the nominal thickness is only a few nanometers, local waviness and thickness fluctuations can appear during deposition and subsequently perturb the optical response of the sensor.

Existing research on roughness in SPR structures has primarily focused on metallic films, coupling surfaces, or dielectric layers other than the top protective overlayer [25–29]. For example, studies by Agarwal et al. [25] and Yang et al. [29] investigated metal roughness using effective medium approaches like the Maxwell-Garnett formulations [30, 31]. Although such models are useful for some interfaces, their accuracy becomes limited when the roughness scale is comparable to the evanescent-field penetration depth at a metal–liquid interface [32].

To the best of the authors' knowledge, little attention has been given to the influence of roughness in a $BaTiO_3$ top protective layer that directly interfaces with the analyte. To analyze the effect of $BaTiO_3$ is important because it is increasingly used to protect Ag while simultaneously enhancing sensitivity. The present study therefore shifts the focus from roughness in the plasmonic metal to roughness in the functional protective overlayer and evaluates whether the associated spectral distortion can be corrected algorithmically.

From a manufacturing perspective, an effective computational correction method (use of the proposed filter) could reduce the dependence on highly expensive, ultra-precise deposition systems. For this reason, the rough surface is modeled here as a periodic waviness profile, following the concept reported by Bai et al. [33]. Thus, instead of relying on Maxwell-Garnett theory and a compound-film effective medium approximation [33]. The analysis considers a nominal $BaTiO_3$ thickness of 3 nm and roughness amplitudes corresponding to a root mean square (RMS) value up to 1 nm, which are representative of thin protective films used in SPR devices.

Any smoothing strategy for SPR spectra must suppress roughness-induced oscillations without erasing the physical features of the resonance dip. Conventional filters such as Gaussian smoothing, Fourier-based denoising, wavelet processing, spline smoothing, and exponentially weighted moving averages can attenuate high-frequency noise, but they may also broaden the SPR minimum, reduce amplitude fidelity, or require simultaneous tuning of multiple spectral descriptors [34–38]. Because top-layer roughness can introduce both low- and high-frequency distortions, a simple low-pass or high-pass treatment alone may be insufficient.

Recent studies show that Savitzky–Golay and Whittaker smoothing can improve spectral quality while preserving key signal features [39–41]. The Savitzky–Golay filter performs local polynomial fitting and is effective when peak shapes must be retained, whereas the Whittaker filter penalizes excessive curvature and often yields stable reconstructions even in the presence of gaps, outliers, or edge effects. These characteristics make both methods suitable candidates for correcting roughness-induced distortion in SPR reflectivity curves.

3. Research Methodology

3.1. SPR sensor structure

Figure 1 illustrates the proposed Kretschmann-type multilayer SPR sensor operating at $\lambda = 632.8$ nm. A CaF_2 prism

Figure 1
A schematic diagram of SPR sensor with surface roughness

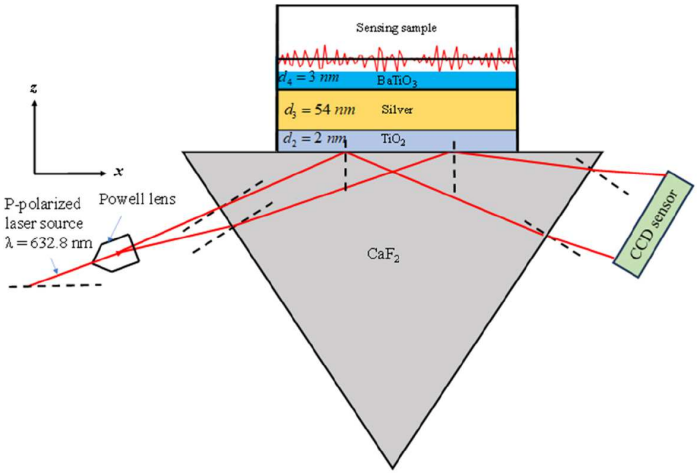

(n = 1.43290) is coated with a TiO_2 layer (n = 2.5836) [42], followed by a 54 nm Ag film that serves as the plasmonic layer. A 3 nm $BaTiO_3$ overlayer (n = 2.4042) is deposited on Ag to protect it from oxidation and to enhance field confinement and sensitivity [20]. The sensing-medium RI is varied from 1.3317 to 1.34. To study fabrication-induced non-uniformity, the top $BaTiO_3$ layer is modeled as a rough surface according to Equation (1).

$$d_{BaTiO_3} = d_{BaTiO_3} + h\sin(n\theta) + h\sin(2n\theta) + h\cos(n\theta_i) + h\cos(2n\theta_i) \quad (1)$$

In Equation (1), the nominal $BaTiO_3$ thickness is perturbed by a periodic function that represents surface waviness. The parameter h denotes the maximum deviation of the local thickness from the mean film thickness and therefore controls the severity of roughness introduced into the optical model.

Figure 2 compares the ideal 3 nm protective layer with the modeled rough profile. While the ideal layer remains constant along the chip surface, the rough profile oscillates approximately between 2.1 and 4.0 nm. This periodic variation is used as a simplified but physically meaningful representation of fabrication-induced top surface roughness in $BaTiO_3$ coatings.

Figure 2
Surface roughness profiles of a protective layer film which was generated based on Equation (1)

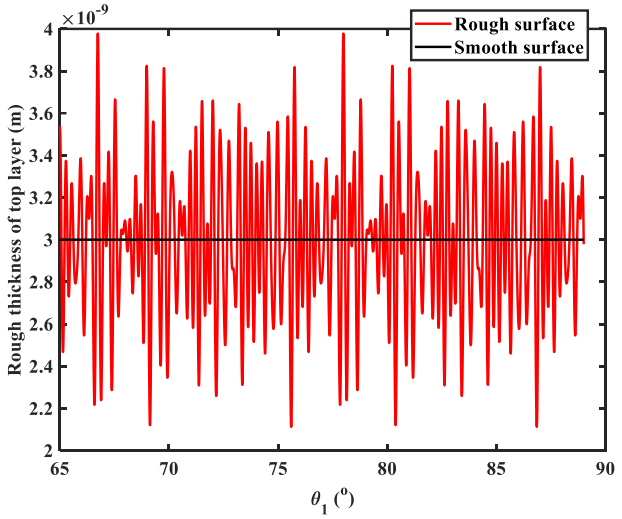

3.2. Mathematical modeling of the multilayer SPR sensor chip

The reflectivity of the multilayer SPR structure is computed using the transfer matrix method, which is well suited to stratified optical media with multiple thin films [43, 44]. In this formulation, the layers are stacked along the z-axis, and each k^{th} layer is characterized by its thickness d_k, RI n_k, and dielectric constant ε_k. By enforcing electromagnetic boundary conditions at each interface, the tangential field components at the first boundary are related to those at the final boundary through the global characteristic matrix [42].

$$\begin{bmatrix} U_1 \\ V_1 \end{bmatrix} = M \begin{bmatrix} U_{N-1} \\ V_{N-1} \end{bmatrix}, \quad (2)$$

In Equation (2), M denotes the total transfer matrix of the multilayer stack, whereas U_1 and V_1 represent the tangential electric and magnetic field components at the first interface, and U_{N-1} and V_{N-1} represent the corresponding fields at the last interface. The matrix therefore propagates the incident wave through the complete sensor structure [42].

$$M_{ij} = \prod_{k=2}^{N-1} \begin{pmatrix} \cos\beta_k & -(i/q_k)\sin\beta_k \\ -iq_k\sin\beta_k & \cos\beta_k \end{pmatrix}_{ij} = \begin{pmatrix} M_{11} & M_{12} \\ M_{21} & M_{22} \end{pmatrix}. \quad (3)$$

Equation (4) defines the transverse-magnetic wave impedance factor q_k for the k^{th} layer. This term determines how strongly the field in each layer contributes to the boundary matching conditions and depends on the optical properties of the layer and the propagation angle.

$$q_k = \frac{\left(n_k^2 - (n_p\sin\theta_i)^2\right)^{1/2}}{n_k^2}, \quad (4)$$

The quantity β_k in Equation (5) is the phase thickness of the k^{th} layer and is proportional to both the physical thickness d_k and the optical path within that layer. Consequently, roughness in the $BaTiO_3$ film changes the phase accumulated by the reflected wave and perturbs the SPR resonance condition [20]:

$$\beta_k = \frac{2\pi d_k}{\lambda}\left(n_k^2 - n_p^2 \sin^2\theta_i\right)^{1/2}. \tag{5}$$

Using the characteristic matrix, the total reflection coefficient for p-polarized (TM) light is obtained from Equation (6). This coefficient contains the combined influence of all interfaces, material refractive indices, and thickness values in the multilayer stack [20]:

$$r^{TM} = \frac{\left(M_{11} + M_{12}q_{sample}\right)q_1 - \left(M_{21} + M_{22}q_{sample}\right)}{\left(M_{11} + M_{12}q_{sample}\right)q_1 + \left(M_{21} + M_{22}q_{sample}\right)} \tag{6}$$

with

$$q_{sample} = \frac{\left(n_{sample}^2 - \left(n_p \sin\theta_i\right)^2\right)^{1/2}}{n_{sample}^2}. \tag{7}$$

Finally, Equation (8) gives the reflectivity power as the squared magnitude of the reflection coefficient. The resonance dip used for performance evaluation is extracted from this reflectivity curve:

$$R = \left|r^{TM}\right|^2 \tag{8}$$

3.3. Filter design

3.3.1. Savitzky–Golay filter design

The Savitzky–Golay filter smooths a noisy SPR spectrum by fitting a low-order polynomial within a moving window centered at each sample point. Its performance depends mainly on two parameters: the window length and the polynomial order. A larger window provides stronger smoothing, whereas a smaller window better preserves narrow spectral features [39, 40, 45].

$$R'_j = \sum_{x=-m}^{m} \frac{C_x R_{j+x}}{N} \tag{9}$$

In Equation (9), R denotes the original SPR reflectance signal, R'_j denotes the smoothed signal, Cx is the convolution coefficient associated with the x^{th} point in the window, and $N = 2m + 1$ is the total number of samples used in the local fit. The index j identifies the current point along the measured spectrum.

The central idea of Savitzky–Golay smoothing is to approximate the local spectrum with an n^{th} order polynomial determined by least squares over the sliding window. Because the fitted polynomial is evaluated at the window center, the method can reduce fluctuations while retaining the local geometry of the resonance dip [39].

$$f(x) = b_0 + b_1 x + b_2 x^2 + \_\_\_\_\_ + b_k x^k \tag{10}$$

In Equation (10), bn represents the polynomial coefficients and k is the polynomial order. These coefficients define the local analytical approximation of the reflectivity data within the selected window.

The coefficients bn are obtained by minimizing the least-squares error between the measured samples and the fitted polynomial, as expressed in Equation (11). This optimization ensures that the smoothed curve remains as close as possible to the original signal in a local sense.

$$\frac{\partial}{\partial b_n}\left\{\sum_{x=-m}^{m}\left[f_k(x) - R_x\right]^2\right\} = 0 \tag{11}$$

After the polynomial coefficients are estimated, the central value b_0 is obtained by evaluating Equation (10) at $x = 0$, which provides the smoothed reflectance at the current position. Higher order derivatives can also be obtained from the fitted polynomial, which is why Savitzky–Golay filtering is widely used for spectral processing and feature preservation.

$$f_k^n(0) = \sum_{x=-m}^{m} C_x^n R_x \tag{12}$$

In Equation (12), n denotes the derivative order, C_x^n is the convolution weight, and R_x is the value of the x^{th} point.

3.3.2. Whittaker filter design

The Whittaker filter formulates smoothing as a penalized least-squares problem in which fidelity to the observed spectrum is balanced against a roughness penalty on the fitted curve. The mathematical expression for the Whittaker filter is given as [46]:

$$Q(\mathbf{z}) = |R(n) - \mathbf{z}|^2 + \lambda_s |D_d \mathbf{z}|^2 \tag{13}$$

In Equation (13), $R(n)$ represents the SPR reflectance corrupted by top protective layer roughness, which is $N \times 1$ of the noised data, $\mathbf{z}$ is the smoothed SPR reflectivity curve for fitting to the noised data, D_d is the second derivative operator, and λ_s is a scalar penalty on the smoothing term. The first term of the objective function preserves agreement with the measured data, whereas the penalty term suppresses rapid curvature changes.

Minimizing Equation (13) with respect to $\mathbf{z}$ yields the estimator in Equation (14). In matrix form, the solution can be interpreted as the result of solving a linear system in which the identity matrix preserves data fidelity and the derivative matrix penalizes excessive oscillation.

$$\hat{\mathbf{z}} = \left(I + \lambda_s D_d^T D_d\right)^{-1} R(n) \tag{14}$$

Accordingly, $R(n)$ and $\mathbf{z}$ denote the nosed spectrum and the smoothed spectrum, respectively; $\boldsymbol{I}$ is the identity matrix, $\boldsymbol{D}_d$ is the differentiation matrix, and d is the derivative order used in the penalty term.

The choice of λ_s is critical. If λ_s is too small, the filtered spectrum remains close to the noisy signal and denoising is weak; if λ_s is too large, the resonance dip may become over-smoothed [46]. Because the optimum value also depends on the number of sampled points, λ_s was tuned empirically, where the larger the number of N, the higher the value of λ_s. In this research, the lambda is chosen to range from $\lambda_s = 10^{10}$ to $\lambda_s = 10^{12}$ for the 24,001 data points spectrum considered in this study, and the optimum value of lambda was around 11^{10}, which yielded the best compromise between noise suppression and preservation of the SPR minimum. The goal of this tuning was to maximize signal-to-noise ratio (SNR) while retaining accurate resonance-angle extraction.

3.4. Designed filters evaluation

The designed filters were evaluated using the SNR, which measures the ability of a method to reduce roughness-induced fluctuations without excessively distorting the underlying SPR signal. The SNR expression used in this study is given in Equation (15) [47].

$$\begin{aligned} SNR &= 10\log_{10}\left(\frac{E_i}{E_n}\right) \\ E_i &= \sum_{n=1}^{N}\left(R_i(n)-\overline{R_i(n)}\right)^2 \\ E_n &= \sum_{n=1}^{N}\left(R_i(n)-R_i'(n)\right)^2 \end{aligned} \tag{15}$$

In Equation (15), E_i is the energy of the ideal SPR signal, E_n is the energy signal of the error or noise component, $R_i(n)$ is the ideal SPR reflectivity without the effect of protective surface roughness, and $R_i'(n)$ is the filtered SPR reflectivity after application of either the Savitzky–Golay or Whittaker filter.

3.5. SPR sensor measurement performance

The SPR sensor performance parameters are extracted from the resonance curve and used to evaluate not only signal smoothness but also sensing quality. The main performance parameters considered here are sensitivity, DA, quality factor (QF), resolution, sensor merit (SM), and combined sensitivity factor (CSF).

3.5.1. Sensitivity

Sensitivity is defined as the ratio of the resonance-angle shift ($\Delta\theta_{res}$) to the corresponding refractive-index change in the sensing medium (Δn_s). It quantifies how strongly the SPR dip responds to variations in analyte RI and is calculated using Equation (16) [48]:

$$S = \frac{\Delta\theta_{res}}{\Delta n_s} \tag{16}$$

3.5.2. Detection accuracy (DA)

DA is inversely proportional to the FWHM of the resonance curve. A narrower reflectivity minimum provides a more precisely localized resonance angle and therefore a higher DA, as expressed in Equation (17) [48]:

$$DA = \frac{1}{FWHM} \tag{17}$$

3.5.3. Quality factor (QF)

The QF combines sensitivity and FWHM to measure how effectively the sensor converts refractive-index changes into a sharp, distinguishable resonance response. A larger QF indicates a more informative and practically useful SPR spectrum [49–51] and has a unit of RIU^{-1}:

$$QF = \frac{S}{FWHM} \tag{18}$$

3.5.4. Resolution

Resolution describes the smallest refractive-index change that can be discriminated by the sensing system. In a charge-coupled device (CCD)-based angular interrogation scheme, the achievable resolution depends on the sensor sensitivity, the number of CCD pixels covering the angular range, and the analog-to-digital conversion precision. In this study, a TCD1304AP linear CCD with 3648 pixels and an STM32F401RE controller with a 12-bit analog-to-digital converter (ADC) are assumed, following [19]:

$$LOD(\sigma_{RI}) = \frac{\sigma_s}{Sensitivity} \tag{19}$$

In Equation (19), σ_s depends on the pixel range covered by the resonance angle, and the ADC conversion resolution $1/(2^n-1)$ is multiplied by the resolution of the CCD. In Equation (19), the overall refractive-index resolution depends on the angular span mapped onto the CCD, the CCD pixel resolution, and the ADC conversion precision. The minimum angular increment that can be distinguished by one pixel is then calculated using Equation (20) [19]:

$$\sigma_s = \frac{\Delta\theta_{res}}{N_{pixel}} \times \frac{1 pixel}{(2^n-1)} \tag{20}$$

N_{pixel} is the total number of pixels of the CCD sensor, and n is the number of bits of the ADC converter.

3.5.5. Sensor merit

SM evaluates the combined influence of resonance sharpness and spectral shape near the minimum. Because it reflects both the width and the contrast of the resonance feature, it is useful for comparing whether a filtering method improves the practical interpretability of the SPR curve [52–54]:

$$SM = \frac{R_{\max} - R_{\min}}{FWHM} \tag{21}$$

3.5.6. Combined sensitivity factor

The CSF is defined as the product of sensitivity and SM. It provides an aggregate measure of how responsive and how spectrally well-defined the sensor response is and is expressed in Equation (22) with units of RIU−1 [54, 55]. Finally, the CSF is expressed as [52, 53], and it has the unit of RIU^{-1}:

$$CSF = S \times SM \tag{22}$$

4. Results and Discussion

4.1. SPR reflectivity curve

Figure 3 was generated using Equation (8), which calculates the total reflectance of P-polarized light after traversing numerous layers with specific optical properties and refractive indices. The SPR reflectance of the ideal and roughened top layers indicates that the ideal layer has a uniform thickness of 3 nm, but the roughened top layer exhibits periodic thickness fluctuations ranging from 2.1 to 4 nm, as referenced in Equation (1). Figure 3(a) and (b) shows the effect of the top-layer roughness on the SPR signal, which is highly irregular, showing significant fluctuations around the SPR dip, which could obscure accurate data interpretation. As shown in Figure 3(a) and (b), roughness introduces oscillatory distortions around the SPR minimum. These distortions arise because local thickness variations modify the optical phase accumulated in the protective layer and therefore perturb the interference condition that determines the resonance dip. As a result, the resonance minimum becomes more difficult to locate reliably, increasing the risk of resonance-angle

Figure 3
SPR reflectivity curve as a function of the incidence angle ranges from 65 to 89° in which (a) has RI = 1.3317 and (b) RI = 1.34

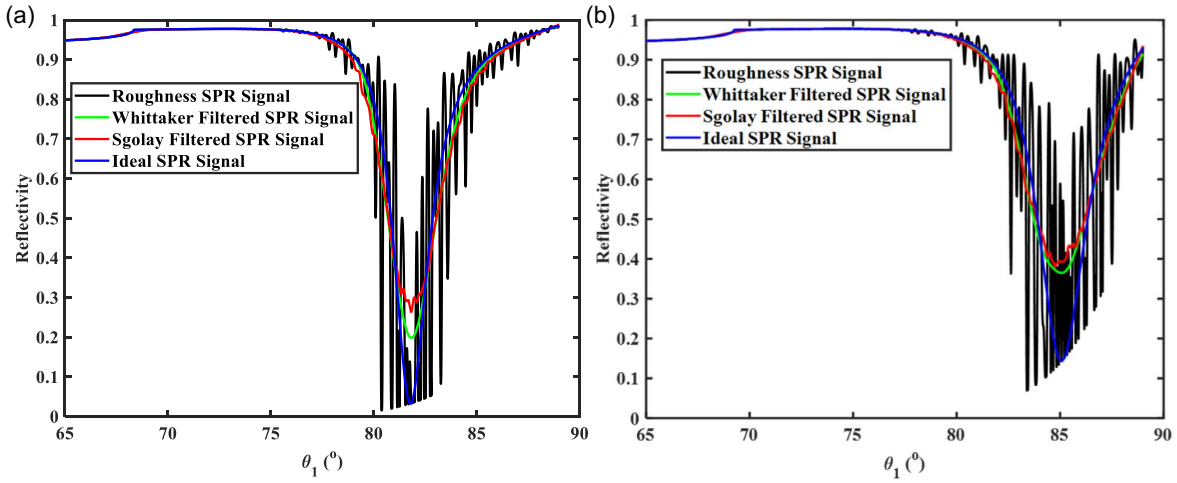

estimation error and degrading downstream metrics such as sensitivity and resolution.

$$\beta_{BaTiO_3} = \frac{2\pi d_{BaTiO_3}}{\lambda}\left(n_{BaTiO_3}^2 - n_p^2 \sin^2\theta_i\right)^{1/2} \tag{23}$$

When the Whittaker filter is applied, the roughness-induced oscillations are substantially suppressed while the underlying resonance shape is preserved. In both RI cases, the Whittaker-smoothed curve follows the ideal SPR dip more closely than the Savitzky–Golay result, especially near the minimum. This behavior is important because accurate extraction of the resonance angle and FWHM depends on preserving the local curvature of the dip. The Savitzky–Golay filter also reduces fluctuations, but it broadens the minimum more noticeably and therefore introduces a higher risk of parameter distortion.

The ideal SPR curve serves as the theoretical reference because it contains a sharp and well-defined minimum in the absence of top-layer roughness. Overall, the comparison indicates that the Whittaker filter is more robust than the Savitzky–Golay filter for handling severe roughness-induced spectral perturbations in the $BaTiO_3$ overlayer.

4.2. SPR sensor performance analysis

Table 1 summarizes the key performance parameters—resolution, sensitivity, FWHM, minimum reflectance, SM, and CSF—for the ideal sensor, the rough sensor, and the two filtered cases. The Savitzky–Golay filter yields the numerically smallest resolution value, 1.986×10^{-7} RIU, but this apparent advantage is associated with stronger reshaping of the resonance dip. By contrast, the Whittaker filter preserves the profile of the ideal resonance more faithfully, which is important for physically meaningful parameter extraction.

Quantitatively, roughness broadens the FWHM from 2.5° for the ideal sensor to 4.3°, indicating a substantial loss of DA. Although the Savitzky–Golay filter suppresses fluctuations, its sensitivity decreases to 357.47°/RIU, which is lower than the rough signal itself (368.55°/RIU) because of dip distortion. The Whittaker filter performs better, maintaining a sensitivity of 390.12°/RIU close to the ideal value of 396.27°/RIU and reducing the FWHM to 3.6° relative to the rough case.

The lowest minimum reflectance occurs for the rough SPR curve (0.045), confirming that roughness alters the resonance depth as well as its position. The ideal curve has a minimum of 0.088, whereas the filtered curves become shallower, with minimum values of 0.281 for the Whittaker filter and 0.323 for the Savitzky–Golay filter. This effect is expected because both filters average neighboring samples. Nevertheless, the Whittaker result remains closer to the physical resonance shape than the Savitzky–Golay result.

The SM values further support this interpretation. The ideal sensor has the highest SM (0.368), indicating the sharpest and most informative resonance signature. The rough case gives SM = 0.224, whereas the Whittaker and Savitzky–Golay filters yield 0.199 and 0.177, respectively. Thus, while filtering improves readability and resonance tracking, it can also reduce spectral sharpness; among the two methods, Whittaker smoothing better balances denoising and feature preservation.

Table 1
Comparative performance metrics for ideal, rough, and filtered SPR sensors

	Resolution ($\times 10^{-7}$) RIU	Sensitivity (°/RIU)	Average FWHM (°)	Average minimum dip (A.U)	SM (A.u/°)	CSF
Ideal SPR	2.202	396.27	2.5	0.088	0.368	146.011
Whittaker filter	2.168	390.12	3.6	0.281	0.199	77.869
SG filter	1.986	357.47	3.8	0.323	0.177	63.165
Roughness SPR	2.048	368.55	4.3	0.045	0.224	82.734

Table 2
Signal-to-noise ratio in dB for SPR roughness, Savitzky–Golay, and Whittaker filter

RI of the sample	SPR_roughness (dB)	Savitzky–Golay filter (dB)	Whittaker filter (dB)
1.3317	5.9271	23.7956	24.958
1.34	6.9137	24.9667	27.919
Average	6.4204	24.3812	26.439

Table 3
Resonance angle for SPR roughness, Savitzky–Golay (SG), and Whittaker filter

RI of the sample	Ideal resonance	Roughness		Savitzky–Golay (SG) filter		Whittaker filter	
	θ_r	θ_{rough}	$\lvert\theta_r - \theta_{rough}\rvert$	θ_{SG}	$\lvert\theta_r - \theta_{SGF}\rvert$	θ_{WHF}	$\lvert\theta_r - \theta_{WHF}\rvert$
1.3317	81.777	80.373	1.404	81.795	0.018	81.823	0.046
1.34	85.066	83.432	1.634	84.762	0.304	85.061	0.005
Average			3.038		0.161		0.0255
Enhancement factor					3.038/0.161 = 18.81		3.038/0.0255 = 119.14

A similar trend is observed for the CSF; the ideal SPR curve yields the highest value (146.011), confirming the expected advantage of a smooth protective layer. Filtering lowers the CSF because shallow dips are penalized in the combined metric, but the filtered results still provide useful practical recovery compared with the distorted rough spectrum. Taken together, the metrics show that Whittaker filtering offers the most reliable overall correction.

4.3. Evaluation of SNR of the SPR sensor

Table 2 reports the SNR for RI = 1.3317 and RI = 1.34. In the rough case, the SNR is only 5.9271 dB at RI = 1.3317 and 6.9137 dB at RI = 1.34, confirming that top-layer roughness substantially degrades signal quality. After filtering, the SNR improves markedly. The Savitzky–Golay filter raises the SNR to about 23.8 dB, whereas the Whittaker filter achieves approximately 24.96 dB. Relative to the rough signal, the Whittaker filter therefore provides an SNR improvement of more than 75%, demonstrating superior suppression of roughness-induced fluctuations while preserving the resonance trend.

4.4. Evaluation of error of resonance position of the SPR sensor

Accurate determination of the resonance angle is one of the most important requirements in SPR sensing. The deviation of the resonance angle from the ideal position was therefore analyzed for the rough and filtered spectra. The Whittaker filter produced an average deviation of only 0.0255°, whereas the Savitzky–Golay filter showed a larger deviation of 0.161°. Relative to the raw rough signal, this corresponds to an improvement factor of 119.14 for the Whittaker filter and 18.81 for the Savitzky–Golay filter, as summarized in Table 3.

5. Conclusion

This study theoretically investigated how physical surface roughness in the $BaTiO_3$ protective layer affects the performance of a Kretschmann-configuration, divergence-beam SPR sensor.

The results show that roughness with an RMS value (height fluctuation) up to 1 nm reduces sensitivity, broadens the FWHM, and lowers the SNR to approximately 6.4 dB. Such degradation can impair resonance-angle estimation and ultimately reduce the reliability of refractive-index sensing in biosensing applications.

Two digital post-processing methods, the Savitzky–Golay filter and the Whittaker filter, were evaluated as mitigation strategies. The comparative analysis shows that the Whittaker filter is superior overall: it improves the resonance-position accuracy by a factor of 119.14 relative to the rough signal, whereas the Savitzky–Golay filter provides an improvement factor of 18.81. In addition, the Whittaker filter increases the SNR by about 75% and preserves the position and shape of the SPR dip more faithfully.

These findings demonstrate that effective digital post-processing can partially relax the strict fabrication tolerances otherwise required to produce a perfectly smooth protective overlayer. In this context, the Whittaker filter offers a practical and low-cost computational alternative for compensating roughness-induced distortion.

The present work is based on theoretical modeling and numerical simulation. Although the transfer matrix method provides a rigorous framework for multilayer analysis, real fabricated chips may exhibit nonperiodic roughness and additional experimental noise sources that are not fully captured by the current model. Future work should therefore focus on experimental validation using fabricated $BaTiO_3$-coated SPR chips and on the implementation of real-time Whittaker-based correction in practical sensing systems.

Acknowledgment

The authors thank the Dar es Salaam Institute of Technology (DIT) for supporting this study.

Ethical Statement

This study does not contain any studies with human or animal subjects performed by any of the authors.

Conflicts of Interest

The authors declare that they have no conflicts of interest to this work.

Data Availability Statement

The data supporting the findings of this study are available within the article, and no external dataset was generated or analyzed.

Author Contribution Statement

Jordan H. Hossea: Conceptualization, Methodology, Formal analysis, Resources, Writing – original draft, Visualization. **Athuman O. Mfinanga:** Software, Validation, Investigation, Writing – review & editing, Supervision.

References

[1] Mondal, H. S., Ahmed, K. A., Birbilis, N., & Hossain, M. Z. (2023). Machine learning for detecting DNA attachment on SPR biosensor. *Scientific Reports*, *13*(1), 3742. https://doi.org/10.1038/s41598-023-29395-1

[2] Jaiswal, L., Dwivedi, D. K., Lohia, P., Mishra, A. C., Yadav, S., & Yadav, R. K. (2024). Numerical study of 2D nanomaterial-based surface plasmon resonance biosensor. *Plasmonics*, *19*(6), 3287–3297. https://doi.org/10.1007/s11468-024-02225-4

[3] Kumar, V., Pal, S., Singh, V., Parajapati, Y. K., & Saini, J. (2024). Design of a highly sensitive and precise long-range surface plasmon resonance sensor for early detection of malaria. *Physica B: Condensed Matter*, *686*, 416072. https://doi.org/10.1016/j.physb.2024.416072

[4] Özgür, E., Topçu, A. A., Yılmaz, E., & Denizli, A. (2020). Surface plasmon resonance based biomimetic sensor for urinary tract infections. *Talanta*, *212*, 120778. https://doi.org/10.1016/j.talanta.2020.120778

[5] Ramaiah, K. B., Suresh, I., Srinandan, C. S., Sai Subramanian, N., & Rayappan, J. B. B. (2024). A dual-sensing strategy for the early diagnosis of urinary tract infections via detecting biofilm cellulose using aromatic amino acid-capped Au and Ag nanoparticles. *Journal of Materials Chemistry B*, *12*(31), 7564–7576. https://doi.org/10.1039/D4TB00902A

[6] Yang, S., Berto, F. G., Denstedt, J., Tang, H., & Zhang, J. (2024). Point-of-care urinary tract infection (UTI) diagnosis enhanced by nanostructured biosensors: Review paper. *Advanced Sensor Research*, *3*(10), 2400051. https://doi.org/10.1002/adsr.202400051

[7] Divya, J., Selvendran, S., Itapu, S., & Borra, V. (2024). A novel dual-channel SPR-based PCF biosensor for simultaneous tuberculosis and urinary tract infection diagnosis toward SDG3. *IEEE Access*, *12*, 85484–85498. https://doi.org/10.1109/ACCESS.2024.3410698

[8] Chiu, N.-F. (2022). The current status and future promise of SPR biosensors. *Biosensors*, *12*(11), 933. https://doi.org/10.3390/bios12110933

[9] Ravindran, N., Kumar, S., Yashini, M., Rajeshwari, S., Mamathi, C A., Thirunavookarasu, S N., & Sunil, C K. (2023). Recent advances in Surface Plasmon Resonance (SPR) biosensors for food analysis: A review. *Critical Reviews in Food Science and Nutrition*, *63*(8), 1055–1077. https://doi.org/10.1080/10408398.2021.1958745

[10] Hojjat Jodaylami, M., Masson, J.-F., & Badia, A. (2025). Surface plasmon resonance sensing. *Nature Reviews Methods Primers*, *5*(1), 47. https://doi.org/10.1038/s43586-025-00417-8

[11] Li, Q., Xu, E., Zhang, X., Tian, J., & Liu, Z. (2025). High-sensitivity Goos-Hänchen shift sensing via surface plasmon resonance and beam displacement amplification. *Sensors*, *25*(5), 1329. https://doi.org/10.3390/s25051329

[12] Rodrigues, M. S., Borges, J., & Vaz, F. (2022). Plasmonic strain sensors based on Au-TiO_2 thin films on flexible substrates. *Sensors*, *22*(4), 1375. https://doi.org/10.3390/s22041375

[13] Hu, Y., Yang, J., Chen, J., Sun, X., Hu, W., & Liu, X. (2025). The development of foodborne pathogen detection and biosensor design for surface plasmon resonance technology. *Biosensors*, *15*(12), 774. https://doi.org/10.3390/bios15120774

[14] Fedorenko, A., Kachur, N., Sulima, O., & Maslov, V. (2024). Protective properties of ZnO nanofilm against wear and mechanical damage of sensitive SPR sensor element. *Functional Materials*, *31*(2), 199–204. https://doi.org/10.15407/fm31.02.199

[15] Sánchez Hernández, H. H., Pérez Abarca, J. M., & Sánchez Soto, E. (2024). Study of surface plasmon resonance with zirconium oxide multilayer coatings of silver and gold films: Reflection polarization modes and sensitivity. *Revista Mexicana de Física*, *70*(2), 021301. https://doi.org/10.31349/RevMexFis.70.021301

[16] Paswan, M. K., & Basu, R. (2025). Comparative study of group-IV materials in SPR sensors: Silicon as an optimized choice based on theoretical analysis. *Silicon*, *17*(15), 3601–3616. https://doi.org/10.1007/s12633-025-03445-x

[17] Li, K., Li, S., Yin, Z., & Li, J. (2024). Experimental study of SPR sensor performance enhancement by metal oxides. *Infrared Physics & Technology*, *136*, 105021. https://doi.org/10.1016/j.infrared.2023.105021

[18] Wang, G., & Huang, L. (2022). Sensitivity enhancement of a silver based surface plasmon resonance sensor via an optimizing graphene-dielectric composite structure. *Applied Optics*, *61*(3), 683–690. https://doi.org/10.1364/AO.446579

[19] Hossea, J. H. (2024). Effect of $BaTiO_3$ and chitosan composite material on the enhancement of the sensitivity and limit of detection of the surface plasmon resonance sensor-divergent beam based. *East African Journal of Information Technology*, *7*(1), 412–426. https://doi.org/10.37284/eajit.7.1.2463

[20] Hossea, J. H., & Rugumira, G. (2024). Analytical design of a portable surface plasmon resonance sensor by using a divergence beam for measuring multiple heavy metals and other contamination simultaneously. *International Journal of Multidisciplinary and Current Research*, *12*(3), 200–207. https://doi.org/10.14741/ijmcr/v.12.3.1

[21] Ishtiak, K. M., Imam, S.-A., & Khosru, Q. D. M. (2022). $BaTiO_3$—Blue Phosphorus/WS2 hybrid structure-based surface plasmon resonance biosensor with enhanced sensor performance for rapid bacterial detection. *Results in Engineering*, *16*, 100698. https://doi.org/10.1016/j.rineng.2022.100698

[22] Mudgal, N., Saharia, A., Agarwal, A., & Singh, G. (2023). ZnO and Bi-metallic (Ag–Au) layers based surface plasmon resonance (SPR) biosensor with $BaTiO_3$ and graphene for biosensing applications. *IETE Journal of Research*, *69*(2), 932–939. https://doi.org/10.1080/03772063.2020.1844074

[23] Mudgal, N., Yupapin, P., Ali, J., & Singh, G. (2020). $BaTiO_3$-graphene-affinity layer–based surface plasmon resonance (SPR) biosensor for Pseudomonas bacterial

detection. *Plasmonics*, *15*(5), 1221–1229. https://doi.org/10.1007/s11468-020-01146-2

[24] Bouandas, H., Kumar, R., Singh, S., Bouazzi, Y., & Sirohi, K. (2025). Enhanced sensitivity and figure of merit in surface plasmon resonance biosensors with silicon dioxide and barium titanate materials. *Microchemical Journal*, *212*, 113341. https://doi.org/10.1016/j.microc.2025.113341

[25] Agarwal, S., Prajapati, Y. K., & Singh, V. (2017). Influence of metal roughness on SPR sensor performance. *Optics Communications*, *383*, 113–118. https://doi.org/10.1016/j.optcom.2016.08.072

[26] Alves, H. P., Castro de Barros, T H., Silva Nascimento, D. L., Peixoto e Sunil, M S., do Nascimento, J. F., Fontana, E., & Martins-Filho, J F. (2022). Influence of surface roughness on the sensitivity of a D-shaped optical fiber-based refractive index sensor. *Sensors and Actuators A: Physical*, *344*, 113702. https://doi.org/10.1016/j.sna.2022.113702

[27] Chen, X., Pan, M., & Jiang, K. (2010). Sensitivity enhancement of SPR biosensor by improving surface quality of glass slides. *Microelectronic Engineering*, *87*(5-8), 790–792. https://doi.org/10.1016/j.mee.2009.11.092

[28] Mitsushio, M., Watanabe, K., Abe, Y., & Higo, M. (2010). Sensor properties and surface characterization of aluminum-deposited SPR optical fibers. *Sensors and Actuators A: Physical*, *163*(1), 1–8. https://doi.org/10.1016/j.sna.2010.07.003

[29] Yang, Z., Liu, C., Gao, Y., Wang, J., & Yang, W. (2016). Influence of surface roughness on surface plasmon resonance phenomenon of gold film. *Chinese Optics Letters*, *14*(4), 042401. https://doi.org/10.3788/COL201614.042401

[30] Chlebus, R., Chylek, J., Ciprian, D., & Hlubina, P. (2018). Surface plasmon resonance based measurement of the dielectric function of a thin metal film. *Sensors*, *18*(11), 3693. https://doi.org/10.3390/s18113693

[31] Sukma, F. O. R., Hanif, M. A., Masruroh, Santjojo., J, D., Apsari, R., Susanto, H., & Tazi, I. (2024). Effects of thickness and roughness on plasmonic characteristics of gold thin films deposited on polished optical fiber. *Materials Research Express*, *11*(1), 016201. https://doi.org/10.1088/2053-1591/ad17eb

[32] Aftab, M., Mansha, M. S., Iqbal, T., & Farooq, M. (2024). Surface plasmon excitation: Theory, configurations, and applications. *Plasmonics*, *19*(4), 1701–1719. https://doi.org/10.1007/s11468-023-02095-2

[33] Bai, Z., Li, M., Zhao, J., Cao, S., Wang, Y., Liao, C., & Wang, Y. (2017). Influence of side-polished fiber surface topography on surface plasmon resonance wavelengths and the full width at half-maximum. *IEEE Photonics Journal*, *9*(2), 4800513. https://doi.org/10.1109/JPHOT.2017.2672898

[34] Hou, R., Wang, Z., Diamond, J., Zheng, Z., Zhu, J., Wang, Z., & Chu, B. (2011). A quantitative evaluation model of denoising methods for surface plasmon resonance imaging signal. *Sensors and Actuators B: Chemical*, *160*(1), 951–956. https://doi.org/10.1016/j.snb.2011.09.010

[35] Boecker, D., Zybin, A., Niemax, K., Grunwald, C., & Mirsky, V. M. (2008). Noise reduction by multiple referencing in surface plasmon resonance imaging. *Review of Scientific Instruments*, *79*(2), 023110. https://doi.org/10.1063/1.2888527

[36] Patskovsky, S., Meunier, M., Prasad, P. N., & Kabashin, A. V. (2010). Self-noise-filtering phase-sensitive surface plasmon resonance biosensing. *Optics Express*, *18*(14), 14353–14358. https://doi.org/10.1364/OE.18.014353

[37] Pavlov, I. N., Vedyashkina, A. V., & Yanina, G. M. (2019). The choice of an image processing algorithm for increasing sensitivity of the surface plasmon resonance method. *Journal of Physics: Conference Series*, *1421*(1), 012012. https://doi.org/10.1088/1742-6596/1421/1/012012

[38] Wang, G., Wang, K., Ren, J., Ma, S., & Li, Z. (2022). A novel doublet-based surface plasmon resonance biosensor via a digital Gaussian filter method. *Sensors and Actuators B: Chemical*, *360*, 131680. https://doi.org/10.1016/j.snb.2022.131680

[39] Kałka, A. J., & Turek, A. M. (2023). Searching for alternatives to the Savitzky–Golay filter in the spectral processing domain. *Applied Spectroscopy*, *77*(4), 426–432. https://doi.org/10.1177/00037028231154278

[40] Schmid, M., Rath, D., & Diebold, U. (2022). Why and how Savitzky–Golay filters should be replaced. *ACS Measurement Science Au*, *2*(2), 185–196. https://doi.org/10.1021/acsmeasuresciau.1c00054

[41] Villarim, M. R., Villarim, A. W. R., Gazziro, M., Cavallari, M. R., Belfort, D. R., & Ando Junior, O. H. (2025). Computational tool for curve smoothing methods analysis and surface plasmon resonance biosensor characterization. *Inventions*, *10*(2), 31. https://doi.org/10.3390/inventions10020031

[42] Singh, S. K., Samanta, U. K., Dhar, A., & Chandra Paul, M. (2021). Structural, morphological, and optical properties of Ag-doped TiO_2 thin-film over fiber optic substrate for sensing applications. *Physica Status Solidi (a)*, *218*(22), 2100447. https://doi.org/10.1002/pssa.202100447

[43] Razmpoosh, M., Namdar, A., & Abdi-Ghaleh, R. (2025). Design and analysis of an improved SPR biosensor utilizing a Mxene sandwich structure for breast cancer cell sensing. *Optical and Quantum Electronics*, *57*(11), 579. https://doi.org/10.1007/s11082-025-08497-2

[44] Vankalayapati, S., Vasimalla, Y., Katakamsetty, A., Vaadaala, J., Ramachandran, B., Santhosh, C., . . . , & Kumar, S. (2025). Design of a dual-metal layer SPR biosensor for enhanced melamine detection using black phosphorus nanomaterials. *Plasmonics*, *20*(7), 5215–5226. https://doi.org/10.1007/s11468-024-02716-4

[45] Rawash, Y. Z., Al-Naami, B., Alfraihat, A., & Owida, H. A. (2024). Advanced low-pass filters for signal processing: A comparative study on Gaussian, Mittag-Leffler, and Savitzky-Golay filters. *Mathematical Modelling of Engineering Problems*, *11*(7), 1841–1850. https://doi.org/10.18280/mmep.110713

[46] Shan, P., Zhi, M., Zhou, J., He, D., Li, Z., He, Z., & Sha, X. (2026). Piecewise fractional differential Whittaker smoother algorithm for ATR-FTIR spectra of complex mixed solutions. *Measurement*, *257*, 118801. https://doi.org/10.1016/j.measurement.2025.118801

[47] Dai, J., & Fu, L. (2024). Denoising of surface plasmon resonance (SPR) spectra using the generalized s-transform and the bald eagle search (BES) algorithm. *Analytical Letters*, *57*(11), 1778–1788. https://doi.org/10.1080/00032719.2023.2272713

[48] Kumar, S., Yadav, A., Kumar, S., & Malomed, B. A. (2024). Design and simulation of SPR sensors by employing silicon and silicon-nitride with mono and bimetal layers for sensitivity enhancement. *IEEE Sensors Journal*, *24*(6), 7671–7680. https://doi.org/10.1109/JSEN.2024.3355766

[49] Bouandas, H., Slimani, Y., Ayadi, K., Ghebouli, M. A., Djemli, A., Fatmi, M., . . . , & Sillanpää, M. (2025). Sensitivity

enhancement of biosensor (SPR) with $PtSe_2$ using Au–Si–Au thin films. *Journal of Optics*, *54*(3), 1043–1051. https://doi.org/10.1007/s12596-024-01807-z

[50] Karki, B., Trabelsi, Y., Pal, A., M, C., Albert, H. M., Sahoo, T., & Gehlot, A. (2025). Design of a silicon and tantalum diselenide-based multilayer surface plasmon resonance sensor for early detection of skin cancer. *Plasmonics*, *20*(12), 11265–11275. https://doi.org/10.1007/s11468-025-03182-2

[51] Singh, K., Kumar, R., Kumar, P., Nehra, V., Gupta, R. K., & Yusuf, M. (2024). Few-layer Si and WS2-based surface plasmon resonance sensor for water salinity concentration detection: Theoretical insight. *Plasmonics*, *19*(6), 3155–3165. https://doi.org/10.1007/s11468-024-02209-4

[52] Mohanan, A., Babu, V. T., Nair, N., Nishi, G., Athulya, S., Arya, K., . . . , & Ram, S. K. (2021). Hybrid design architecture and sensitivity analysis of Cu based surface plasmon resonance sensors. *Research Transcripts in Materials*, *1*, 17–34.

[53] Ceballos-Zumaya, J., Sustaita-Torres, I. A., Pérez-Huerta, J. S., Ariza-Flores, D., & Madrigal-Melchor, J. (2024). Performance parameters as a function of graphene's chemical potential for SPR biosensor based on 2D materials. *Optik*, *314*, 172013. https://doi.org/10.1016/j.ijleo.2024.172013

[54] Das, S., Prava Mondal, T., Kumar Roy, K., Reza Mahmud, R., Shariful Islam, M., & Barua, B. (2025). Design and optimization of an SPR-based biosensor with ultra-high sensitivity using a hybrid structure for accurate dengue virus detection. *Plasmonics*, *20*(11), 10243–10262. https://doi.org/10.1007/s11468-025-03107-z

[55] Shivangani, Sahu., Kumar, A., Verma, D., Chauhan, S., S, S., Tiwari, R. K., & Kumar, S. (2025). Design and analysis of surface plasmon resonance sensor utilizing silver, nickel, and black phosphorous for various cancer detection. *Plasmonics*, *20*(8), 6623–6639. https://doi.org/10.1007/s11468-025-02961-1

How to Cite: Hossea, J. H., & Mfinanga, A. O. (2026). Mitigating Surface-Roughness Effects in the $BaTiO_3$ Top Protective Layer of a Divergence Beam Surface Plasmon Resonance Sensor Using Savitzky–Golay and Whittaker Filters. *Journal of Optics and Photonics Research*. https://doi.org/10.47852/bonviewJOPR62028166